Tuning of multiferroic order with Co doping in $CuCr_2O_4$: Interplay between structure and orbital order

A. Chatterjee,[1] J. K. Dey,[1] S. Majumdar,[1] A.-C. Dippel,[2] O. Gutowski,[2] M. v. Zimmermann,[2] and S. Giri[1,*]
[1]*School of Physical Sciences, Indian Association for the Cultivation of Science, Jadavpur, Kolkata 700032, India*
[2]*Deutsches Elektronen-Synchrotron, Notkestraße 85, 22607 Hamburg, Germany*

(Received 26 July 2019; revised manuscript received 30 August 2019; published 8 October 2019)

We observe a ferroelectric (FE) order in an unexplored $CuCr_2O_4$ with a reasonably high value of the FE Curie temperature (T_{FE}) at 170 K, which is also much higher than the magnetic ordering temperature. The systematic substitution of Jahn-Teller (J-T) active divalent Cu ion by a non-Jahn-Teller active divalent Co ion causes a systematic shift of T_{FE} from 170 K for $x = 0$ to 146 K for $x = 0.8$ in $Cu_{1-x}Co_xCr_2O_4$. The values of electric polarization vary from 0.0665 $\mu C\,cm^{-2}$ to 0.1704 $\mu C\,cm^{-2}$, which is maximum for $x = 0.6$, associated with the highest value of the coercivity. The synchrotron diffraction studies of the compounds with $x = 0.2$ and 0.8 confirm that a structural transition to a polar $Ima2$ space group from the tetragonally distorted $I4_1/amd$ structure gives rise to the ferroelectricity. In all the members of $Cu_{1-x}Co_xCr_2O_4$ series, the T_{FE} is observed at much higher temperature than the corresponding magnetic ordering temperatures (T_N). These results are in contrast to that of the reported results of $T_{FE} < T_N$ for the end member with $x = 1$ or $CoCr_2O_4$, where the J-T active Cu^{2+} is absent. We propose that the J-T distortion in the entire series with $0 \leqslant x \leqslant 0.8$ holds the key, where interplay between the J-T distortion driven orbital order and the structural distortion correlates tuning of the T_{FE} in $Cu_{1-x}Co_xCr_2O_4$.

DOI: 10.1103/PhysRevMaterials.3.104403

I. INTRODUCTION

Over the past few decades, the delicate interplay among the charge, spin, orbital, and lattice degrees of freedom provides many rich consequences. One of the fascinating outcomes is the colossal magnetoresistance in the mixed-valent manganites [1,2]. Moreover, this intricate interplay gives rise to the diverse ranges of the interesting magnetic properties from the frustrated magnetism to the multiferroic properties [3–8]. In the above cases, the orbital ordering driven by the the Jahn-Teller (J-T) distortion has been found crucial, which was intimately correlated to the structural distortion and also, eventually, directed the magnetic properties.

Recently, the J-T effect driven occurrence of multiferroic order has been proposed for ABO_3-type perovskite [9] including $RMnO_3$ [10] and $RNiO_3$ [11]. The interplay among J-T effect, orbital ordering, structural instability, and ferroelectricity has been proposed for A-site ordered double perovskite $CaMnTi_2O_6$ [12] and spin-chain compound Ca_3CoMnO_6 [13]. The AB_2O_4-type spinel compound, $CuCr_2O_4$, attracts the community for the Cu^{2+} ions at the tetrahedral site, where the Cu^{2+} with $3d^9$ electronic configuration is strongly a J-T active ion [14,15]. An example of a tetrahedral unit connected with a CrO_6 octahedron within the general representation of a cubic structure is depicted in Fig. 1(a) having a $Fd\bar{3}m$ space group. The four corners of a tetrahedron are occupied by the oxygen ions (O^{2-}), whereas the Cr^{3+} ions occupy the octahedral site with the six O^{2-} sitting at the corners of a octahedron, as also depicted in Fig. 1(a). Because of the distortion of the CuO_4 tetrahedra driven by the J-T effect, as depicted in Fig. 1(b), the degeneracies of the e_g and t_{2g} orbitals are lifted, resulting in the ordering of the d orbitals, which is shown in Fig. 1(c). The compound crystallizes in the cubic structure with the $Fd\bar{3}m$ space group above 853 K, below which the compound undergoes a structural transition to a tetragonal structure with the $I4_1/amd$ space group [14,16–24]. The CuO_4 tetrahedra in the tetragonal structure are compressed into a square planar structure, resulting from the J-T effect. The magnetic and structural transition, and infrared spectroscopy, proposed concomitant occurrence of ferrimagnetic order (T_N) and structural transition in $CuCr_2O_4$, suggesting a strong magnetoelastic coupling [7,8,25,26]. The neutron scattering studies proposed a magnetic structure with a moment of 0.5 μ_B per formula unit, where two canted Cr^{3+} sublattices and one Cu^{2+} sublattice were coupled antiferromagnetically below T_N [18,23,24]. The $^{63,65}Cu$ and ^{53}Cr nuclear magnetic resonance studies further confirmed that the angle between the Cr^{3+} and the Cu^{2+} magnetic moments was found to be ≈98° [5]. Furthermore, the spin-orbit coupling of Cr ions was proposed to be much stronger than that of Cu ions related to the orbital ordering in $CuCr_2O_4$.

In the present work, we report an unexplored ferroelectric (FE) order with a significant value of polarization of ≈0.15 $\mu C\,cm^{-2}$ for $CuCr_2O_4$. Here, the ferroelectric order is observed at much higher temperature than the magnetic order with a FE Curie temperature (T_{FE}) of ≈170 K. The doping of Cu^{2+} with Co^{2+} systematically tunes the T_{FE} as well as magnetic ordering temperature (T_N), which decreases with increasing x in $Cu_{1-x}Co_xCr_2O_4$. The synchrotron diffraction studies of the two representative compounds with $x = 0.2$ and 0.8 clarify the occurrence of the ferroelectric order. A structural transition to a polar structure with a $Ima2$ space group from the centrosymmetric tetragonal structure with the

---

[*] Corresponding author; sspsg2@iacs.res.in

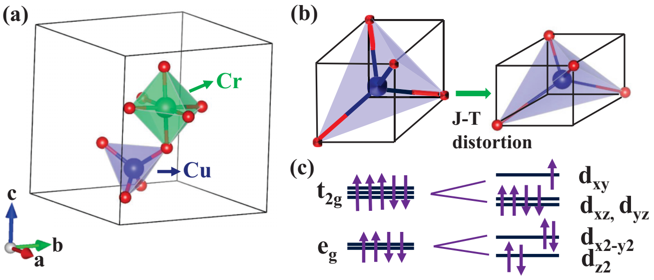

FIG. 1. (a) Connecting Cr octahedron and Cu tetrahedron within the unit cell. (b) Distortion of CuO_4 tetrahedra driven by the J-T effect. (c) Lifting of orbital degeneracy of *d* orbitals in the tetrahedral coordination due to J-T effect.

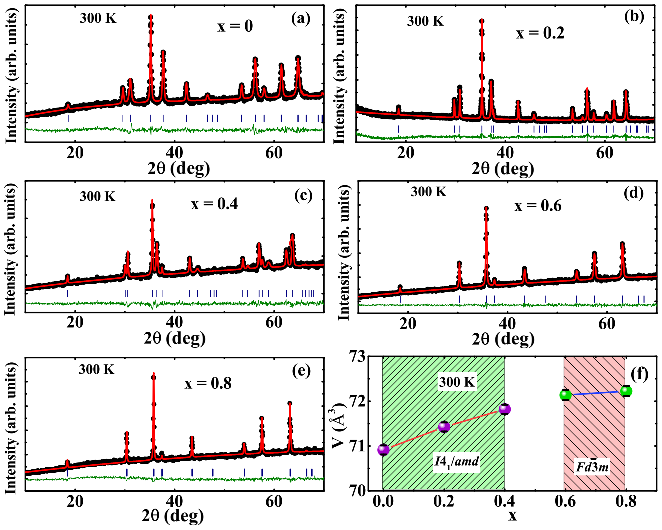

FIG. 2. Rietveld refinement of x-ray diffraction patterns of $Cu_{1-x}Co_xCr_2O_4$ for x = (a) 0, (b) 0.2, (c) 0.4, (d) 0.6, (e) 0.8 respectively at 300 K. (f) Variation of the volume of the unit cell at room temperature. For $x = 0$, 0.2, and 0.4, the structure is fitted with the tetragonal $I4_1/amd$ and for $x = 0.6$ and 0.8 with the cubic $Fd\bar{3}m$ structures.

$I4_1/amd$ space group is observed around T_{FE}. The possible correlation of the J-T distortion with the observed structural-transition-driven occurrence of the FE order are discussed for $Cu_{1-x}Co_xCr_2O_4$.

II. EXPERIMENTAL DETAILS

The polycrystalline compounds with the chemical formula of $Cu_{1-x}Co_xCr_2O_4$ for $0 \leqslant x \leqslant 0.8$ are prepared by the solid-state reactions [27]. The single-phase chemical composition is confirmed by the x-ray diffraction studies at room temperature recorded in a PANalytical x-ray diffractometer (Model: X'Pert PRO) using the Cu Kα radiation. The single-phase chemical composition is further verified by the synchrotron x-ray diffraction studies recorded with a wavelength of 0.14235 Å (87.1 KeV) at the P07 beamline of PETRA III, Hamburg, Germany, using a two-dimensional (2D) Perkin Elmer detector in the temperature range of 10–300 K. Analysis of these synchrotron powder diffraction data are done using the Rietveld refinement with the commercially available MAUD and FULLPROF software. The powder samples pressed into pellets are used for the dielectric measurements using a E4980A LCR meter (Agilent Technologies, USA) equipped with a PPMS-II system of Quantun Design. The pyroelectric current (I_p) is recorded in an electrometer (Keithley, model 6517B) by sweeping temperature at a constant rate. The I_p is integrated with time for obtaining spontaneous electric polarization (P). The sample is poled with different electric fields during the cooling process. Thereafter, all the electrical connections across the sample are short circuited for an hour or more, before the measurements of I_p are carried out in the warming mode in zero electrical field. It is noted that in all the measurements, the electrical contacts are fabricated using an air-drying silver paint. The dc magnetization is measured in a commercial magnetometer of Quantum Design (MPMS, evercool), where the dc magnetization is recorded in both the zero-field-cooled (ZFC) and field-cooled (FC) protocols.

III. EXPERIMENTAL RESULTS AND DISCUSSION

The x-ray diffraction patterns of the powder samples of $Cu_{1-x}Co_xCr_2O_4$ with $x = 0$, 0.2, 0.4, 0.6, 0.8 are recorded at 300 K. Herein, the results for $x = 0$ reproduce the previous reports of $CuCr_2O_4$ [14,16–24]. All x-ray diffraction patterns are analyzed by using the Rietveld refinement with the tetragonal structure with the $I4_1/amd$ space group for $x \leqslant 0.4$ and cubic structure with the $Fd\bar{3}m$ space group for $0.6 \leqslant x \leqslant 0.8$, as shown in Figs. 2(a)–2(e). Figure 2(f) shows the variation of the unit cell volume (V) with x, where the $V(T)$ shows an increasing trend with increasing the Co doping. The result is reasonable, because the divalent Co ion has higher value of the ionic radius than that of the divalent Cu ion. The bars below the diffraction patterns show the peak positions. The difference plots at the bottom of the diffraction patterns in Figs. 2(a)–2(e) confirm the absence of any additional impurity peak, where the reasonable fits are indicated by the decent ranges of the reliability parameters, R_w (%) = 4.0–5.05, R_{exp} (%) = 2.4–3.0, and χ^2= 2.1–1.9.

Thermal variations of the ZFC and FC magnetization (M) curves recorded at 1 kOe are displayed in Figs. 3(a)–3(e) for $Cu_{1-x}Co_xCr_2O_4$ with $x = 0$, 0.2, 0.4, 0.6, 0.8. Figure 3(a) shows the temperature dependence of magnetization for $CuCr_2O_4$ measured in the ZFC and FC protocol, as reported earlier [3]. The first T derivative of magnetization (not shown in the figure) provides the value of T_N. The values of T_N, as determined from the derivative plot, are listed in Table I and also depicted in Fig. 3(f). The value of T_N is close to that observed in the previous reports [3,28]. The value of T_N decreases with increasing x. The $M(T)$ results for $x = 0.2$, 0.4, 0.6, and 0.8 are plotted in Figs. 3(b)–3(e), respectively, displaying different characteristic features. The reversal of magnetization in the thermal variation of the ZFC curve is observed for $x = 0.2$ and 0.8. The ZFC curve for $x = 0.2$ becomes negative below ≈80 K and remains negative, showing a decreasing trend. For $x = 0.8$, the $M(T)$ also changes sign around ≈70 K and it becomes positive below ≈35 K, which is consistent with the previous reports measured at different magnetic fields [25,29]. The FC curve of the compound with $x = 0.6$ exhibits a change in sign around ≈80 K and remains

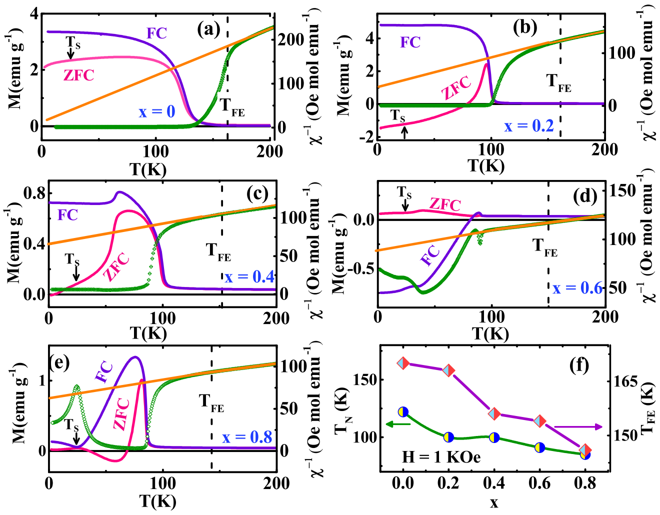

FIG. 3. Temperature (T) variations of the FC-ZFC magnetization for $Cu_{1-x}Co_xCr_2O_4$ for x = (a) 0, (b) 0.2, (c) 0.4, (d) 0.6, (e) 0.8. Right axis shows the corresponding inverse susceptibility χ^{-1} (T) and the Curie-Weiss fit. (f) Plot of magnetic ordering temperatures (T_N) and ferroelectric Curie temperatures (T_{FE}) with x.

negative until 2 K. In accordance with the previous reports, these are the usual characteristics of the ferrimagnetically ordered state, where the compensation of magnetization along the magnetic field leads to the change in sign of $M(T)$ [27,30–32].

The inverse susceptibilities (χ^{-1}) measured in the FC protocol with T are shown in the right axis of Figs. 3(a)–3(e) for all the compositions. The linear fit using Curie-Weiss law is displayed by a straight line for each curve. From the high-temperature linear Curie-Weiss fit, the effective paramagnetic moment (μ_{eff}) and Curie-Weiss temperature (Θ_{CW}) are obtained, which are listed in Table I, along with the theoretical values (μ_{theo}). The theoretical values of μ_{eff} are calculated using the following equation [33]:

$$\mu_{\text{eff}} = \sqrt{(1-x)\mu^2_{\text{Cu}^{2+}} + x\mu^2_{\text{Co}^{2+}} + 2\mu^2_{\text{Cr}^{3+}}}. \tag{1}$$

We note that the values of μ_{eff} are satisfactorily close to the corresponding values of μ_{theo} for x 0 and 0.2. The values of μ_{eff} are larger than the values of μ_{theo} for the rest of the members. The μ_{eff}, as obtained from the higher temperature Curie-Weiss fit for these compounds, are suggested for the satisfactory matching with the μ_{theo} values. The value of Θ_{CW}/T_N ratio is close to 1 for $x = 0$ and it increases with increasing x, pointing to an increase of magnetic frustration. The value of the ratio is maximum for $x = 0.6$.

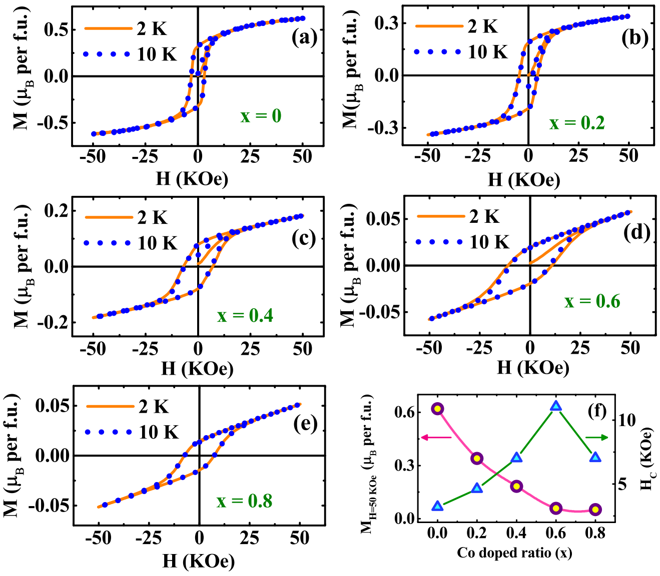

FIG. 4. Magnetic hysteresis loops at 2 and 10 K for $Cu_{1-x}Co_xCr_2O_4$ with x = (a) 0, (b) 0.2, (c) 0.4, (d) 0.6, (e) 0.8, respectively. (f) Left axis shows the magnetization values at H = 50 KOe and right axis shows the values of coercivity with x.

Figures 4(a)–4(e) depict the magnetic hysteresis loops recorded at 2 and 10 K for all the compositions. We note that the loops at 2 and 10 K nearly overlap for all the compositions, except for $x = 0.6$, where the coercivity (H_C) slightly decreases at 10 K. In all the cases, the magnetization does not saturate at 50 kOe. The values of magnetization at 50 kOe ($M_{\text{H=50 kOe}}$) and H_C are plotted with x, as depicted in Fig. 4(f). The value of $M_{\text{H=50 kOe}}$ decreases systematically with increasing x. The H_C also increases with increasing x and shows a maximum at $x = 0.6$, below which it shows a decreasing trend. The highest coercivity might be correlated to the highest magnetic frustration for $x = 0.6$.

The dielectric permittivity (ϵ) is recorded at different frequencies (f) by varying T for all the compositions. Figures 5(a)–5(e) shows the thermal variation of real component of dielectric permittivity (ϵ') for x = 0, 0.2, 0.4, 0.6, and 0.8, respectively. In Fig. 5(a), a steplike change in $\epsilon'(T)$ is noticed around 170 K, at which the FE Curie temperature is observed for the parent compound. The results of the FE order for the entire series are discussed below. The signature of T_{FE} in $\epsilon'(T)$ is also evident for $x = 0.2$ and 0.4 and is

TABLE I. Magnetic and ferroelectric parametrs of $Cu_{1-x}Co_xCr_2O_4$ at different x.

			Magnetic			Ferroelectric	
x	T_N (K)	Θ_{CW} (K)	$\lvert\Theta_{\text{CW}}/T_N\rvert$	μ_{eff} (μ_B)	μ_{theo} (μ_B)	T_{FE} (K)	P (μC cm^{-2})
0	122	−115	0.94	3.24	3.71	170	0.1423
0.2	100	−136	1.36	4.21	4.45	168	0.1384
0.4	99	−250	2.52	6.41	5.77	156	0.1124
0.6	91	−527	5.79	7.10	5.64	154	0.1704
0.8	85	−346	4.07	6.75	6.15	146	0.0665

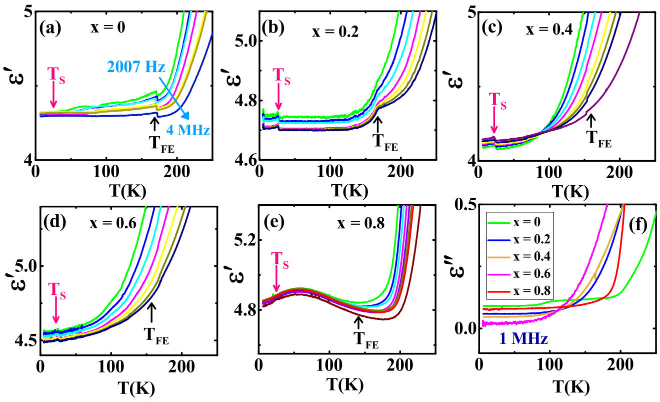

FIG. 5. The T variations of ϵ' at different f in the range of 2007 Hz to 4 MHz for $Cu_{1-x}Co_xCr_2O_4$ with $x =$ (a) 0, (b) 0.2, (c) 0.4, (d) 0.6, (e) 0.8, respectively. (f) T variation of ϵ'' at $f =$ 1MHz.

not detectable for $x = 0.6$ and 0.8. In addition, another low-T anomaly (T_s) is observed for $x = 0.2$, 0.4, 0.6, and 0.8, which is not so evident in the $M(T)$ curve. The signature of T_s is not detectable for the parent compound. However, a weak change of slope in the ZFC curve may be correlated to the low-T anomaly in $\epsilon'(T)$, pointing to a magnetoelectric coupling. The low-T anomaly is attributed to the spiral magnetic order, as suggested in the previous reports [25,27,29–32]. In Fig. 5(f), the imaginary components (ϵ'') are depicted for all the compositions.

To confirm the FE order, the values of I_p are recorded with T for all the compositions. A peak in $I_p(T)$ is observed for all the samples, as evident in Figs. 6(a)–6(e) for $x = 0$, 0.2, 0.4, 0.6, and 0.8, respectively. Here, the $I_p(T)$ is measured for the two different rates of 3 and 5 K/min. A sharp peak in the $I_p(T)$ curve is observed at ≈170, ≈168, ≈155, ≈154, and 146 K for $x = 0$, 0.2, 0.4, 0.6, and 0.8, respectively. The integral of $I_p(T)$ over time gives the value of $P(T)$. We note that the I_p recorded at different heating rates provides a reproducible value of P with T. The thermal variations of P for different poling fields (E) and both for the positive and negative E are depicted in Figs. 6(f)–6(j). The reversal of $P(T)$ due to a change in sign of E (±5 kV/cm) signifies the ferroelectric order [34–37]. The P values increase with E, pointing to the fact that the P does not saturate for E at −5 kV/cm for $x = 0$, 0.6, and 0.8. The P values saturate at 5 kV/cm for $x = 0.2$ and 0.4. The values of P are considerable and vary from 0.0665 to 0.1704 $\mu\mathrm{C\,cm^{-2}}$ for $E = 5$ kV/cm, as listed in Table I. We note that the value of P is maximum for $x = 0.6$, where the maximum values of Θ_{CW}/T_N ratio and coercivity are observed. The results are significant, because the large strain attributed to the structural distortion may lead to the enhancement of the coercivity. This strain may direct the increase of the polarization value [36,38–40]. The detailed structural studies of the compound with $x = 0.6$ will confirm it. The value of P reduces significantly for $x = 0.8$ with the maximum content of Co. Nevertheless, the values of P for the rest of the members of the $Cu_{1-x}Co_xCr_2O_4$ series are quite large compared to the polarization values of the promising multiferroics [40–43]. To find out the origin of the ferroelectric order much above the magnetic ordering temperature, the structural properties are investigated by the synchrotron diffraction studies over a temperature range of 10–300 K for the two representative compounds with $x = 0.2$ and 0.8.

In accordance with the previous reports [21,26], the diffraction pattern at 300 K of the sample with $x = 0.2$ is refined using the $I4_1/amd$ space group, as depicted in Fig. 2(b). The refined atomic positions are given in Table II. Temperature variation of the integrated intensity of the (101) diffraction peak is depicted in Fig. 7(a), which displays the anoma-

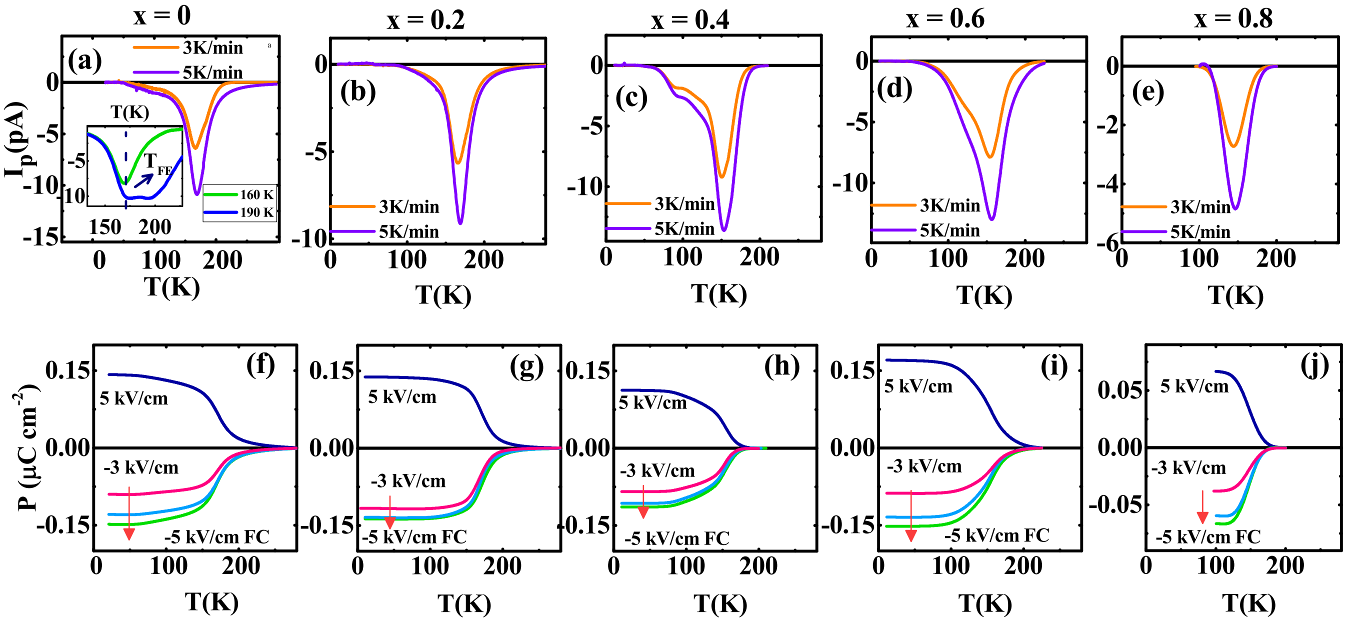

FIG. 6. The T variations of the pyroelectric current (I_p) at two different thermal sweep rates with a −5 kV/cm poling field for $Cu_{1-x}Co_xCr_2O_4$ with $x =$ (a) 0, (b) 0.2, (c) 0.4, (d) 0.6, (e) 0.8 and the corresponding electric polarization (P) with T for $x =$ (f) 0, (g) 0.2, (h) 0.4, (i) 0.6, (j) 0.8.

TABLE II. Atomic positions associated with the structural parameters of $Cu_{1-x}Co_xCr_2O_4$ for $x = 0.2$ and 0.8. O* stands for the occupancy.

T (K)	Space group	Atoms	x	y	z	O*	Site
			$x = 0.2$				
300	$I4_1/amd$	Cu	0	0.25	0.375	0.8	4b
		Co	0	0.25	0.375	0.2	4b
		Cr	0	0	0	1.0	8c
		O	0	0.5364(0)	0.2526(0)	1.0	16h
100	$Ima2$	Cu	0.25	0.375	0	0.8	4b
		Co	0.25	0.375	0	0.2	4b
		Cr1	0	0	0	1.0	4a
		Cr2	0.25	0.75	0.25	1.0	4b
		O1	0.5392(9)	0.25	0	1.0	8c
		O2	0.25	0.5	0.7100(8)	1.0	4b
		O3	0.25	0	0.7703(0)	1.0	4b
			$x = 0.8$				
300	$Fd\bar{3}m$	Cu	0.375	0.375	0.375	0.2	8b
		Co	0.375	0.375	0.375	0.8	8b
		Cr	0.25	0.25	0	1.0	16c
		O	0.2380(3)	0.2380(3)	0.2380(3)	1.0	32e
200	$I4_1/amd$	Cu	0	0.25	0.375	0.2	4b
		Co	0	0.25	0.375	0.8	4b
		Cr	0	0	0	1.0	8c
		O	0	0.5370(3)	0.2515(1)	1.0	16h
100	$Ima2$	Cu	0.25	0.375	0	0.2	4b
		Co	0.25	0.375	0	0.8	4b
		Cr1	0	0	0	1.0	4a
		Cr2	0.25	0.75	0.25	1.0	4b
		O1	0.5387(7)	0.25	0	1.0	8c
		O2	0.25	0.5	0.7069(5)	1.0	4b
		O3	0.25	0	0.7705(7)	1.0	4b

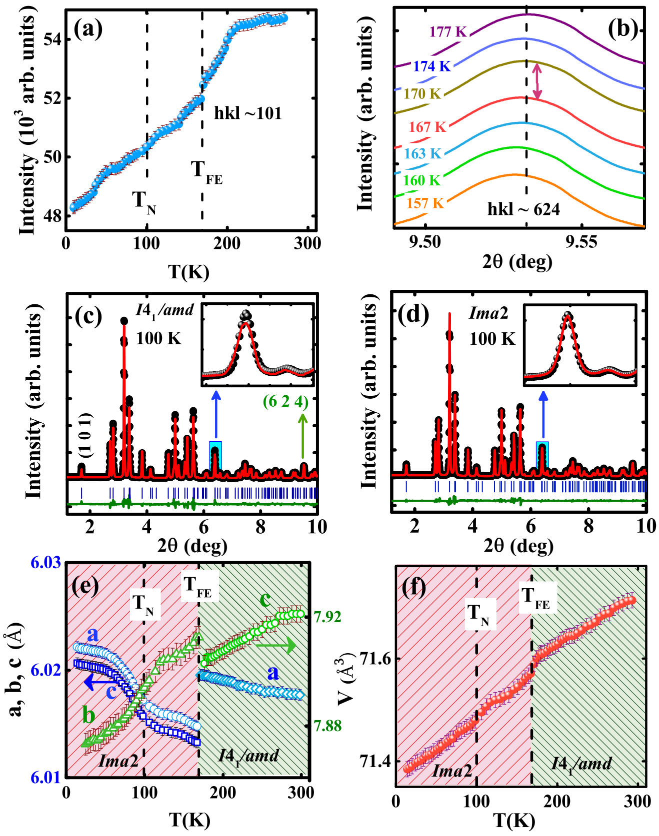

FIG. 7. (a) The T variation of the integrated intensity of the (101) peak. (b) The magnified (101) peak at different temperatures around T_{FE}. The Rietveld refinements of the diffraction pattern at 100 K using (c) $I4_1/amd$ and (d) $Ima2$ space groups. Insets of panels (c) and (d) further highlight the quality of the refinements in a small 2θ region. The T variation of (e) lattice parameters a and c and (f) the unit cell volume (V) for $x = 0.2$.

lies at T_N and T_{FE} around ≈100 and ≈168 K, respectively, as also indicated by the vertical broken lines in the figure. Here, the signature of T_{FE} in the integrated intensity plot is correlated to the structural transition, as reported earlier [35,40,41]. A selected 2θ region of the diffraction peaks around T_{FE} is highlighted in Fig. 7(b). The figure indicates a small shift in the peak position and the change in the intensity around T_{FE}. We note that the refinement using $I4_1/amd$ space group is not satisfactory below T_{FE}. An example of the refinement of the diffraction pattern at 100 K using the $I4_1/amd$ space group is depicted in Fig. 7(c). Inset magnifies a small 2θ region of the pattern, indicating a significant mismatch in the refinement process. We incorporate ISODISTORT [44] software to find out the possible polar space group, which can fit with the diffraction patterns below the T_{FE}, to address the FE order above the magnetic order. The best fit is obtained for the $Ima2$ (46) space group. The better refinement of the diffraction pattern using the $Ima2$ space group at 100 K is shown in Fig. 7(d) with the small reliability parameters, R_w (%) ∼ 3.3, R_{exp} (%) ∼ 2.1, and χ^2 ∼ 2.0. Inset of the figure magnifies a small 2θ region and confirms the satisfactory fit. The refined coordinates of the atoms at 100 K are listed in Table II.

Thermal variations of the lattice parameter, a, b, and c, as obtained from the refinements, are depicted in Fig. 7(e). We note a structural transition to a polar structure of $Ima2$ space group from the $I4_1/amd$ structure, as highlighted in the figure by the different regions separated by a vertical broken straight line. The lattice constant c at high temperature converts to the b axis at low temperatures below T_{FE} and keeps on decreasing with the decrease in temperature. In contrast to the decrease of c, the lattice constant a in the high-temperature region increases with the lowering of temperature down to T_{FE} and it undergoes a steplike decrease at T_{FE}. Below T_{FE}, it splits into new lattice constants such as a and c, which continue to increase until the lowest temperature. The changes in the slopes of $a(T)$, $b(T)$, and $c(T)$ are evident around T_N, indicating a magnetoelastic coupling. The calculated unit cell volume (V) is plotted with T in Fig. 7(f). The $V(T)$ decreases with decreasing temperature, exhibiting a discontinuous change at T_{FE} and an anomaly close to T_N. To investigate the deformation at the structural transition, the bond lengths and bond angles are measured by varying the temperatures.

The $Ima2$ space group allows one Cu atom, two Cr atoms (Cr1 and Cr2), and three O atoms (O1, O2, and O3) in the structure. The tetrahedral site occupied by Cu^{2+} ion is

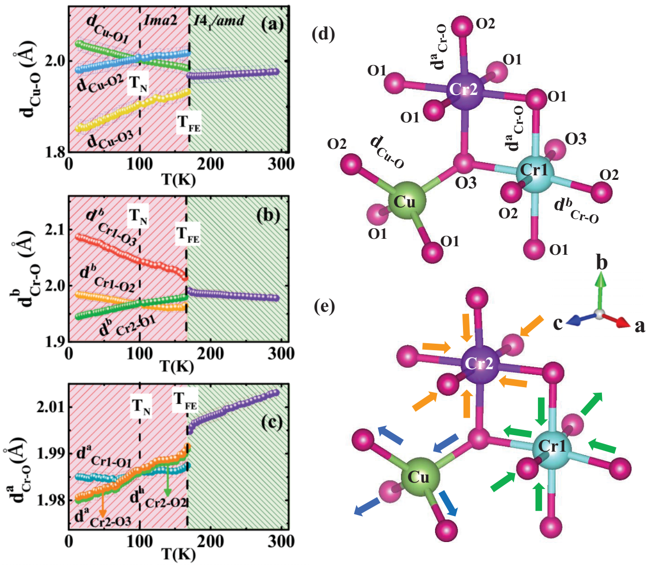

FIG. 8. Temperature variations of the (a) Cu-O bond length ($d_{\mathrm{Cu-O}}$), (b) basal Cr-O bond length ($d^b_{\mathrm{Cr-O}}$), and (c) apex Cr-O bond length ($d^a_{\mathrm{Cr-O}}$) with T. Schematic representations of the (d) connecting $\mathrm{CuO_4}$ tetrahedron and $\mathrm{CrO_6}$ octahedra and (e) their distortions at T_{FE} for $x = 0.2$.

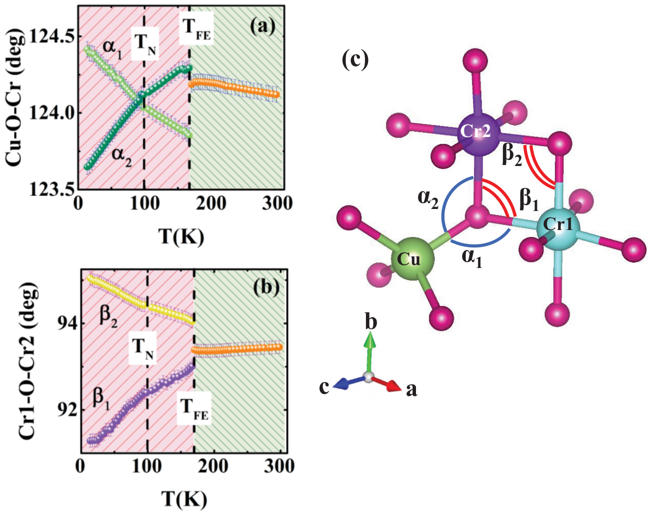

FIG. 9. The T variations of the (a) Cu-O-Cr and (b) Cr-O-Cr bond angles. (c) Schematic representation of the details of the bond angles for $x = 0.2$.

connected with four oxygen atoms, whereas the $\mathrm{Cr^{3+}}$ ion occupies the octahedral site and six oxygen are sitting at the corners of the octahedra. The connecting two $\mathrm{CrO_6}$ octahedra and one $\mathrm{CuO_4}$ tetrahedron are depicted in Fig. 8(d). The $\mathrm{Cu^{2+}}$ in a tetrahedron is connected with O1, O2, and O3 below T_{FE} and the corresponding bond lengths are defined as $d_{\mathrm{Cu-O1}}$, $d_{\mathrm{Cu-O2}}$, and $d_{\mathrm{Cu-O3}}$, respectively. Here, $\mathrm{CuCr_2O_4}$ is the parent compound and $\mathrm{Co^{2+}}$ substitutes the $\mathrm{Cu^{2+}}$ ion. For simplicity, we discuss only $\mathrm{CuO_4}$ in place of $\mathrm{(Cu/Co)O_4}$ tetrahedra. In the case of $\mathrm{CrO_6}$ octahedra, the apex and basal bond lengths are defined as $d^a_{\mathrm{Cr-O}}$ and $d^b_{\mathrm{Cr-O}}$, respectively. Thermal variations of the $d_{\mathrm{Cu-O1}}$, $d_{\mathrm{Cu-O2}}$, and $d_{\mathrm{Cu-O3}}$ are depicted in Fig. 8(a). At the structural transitions, the $d_{\mathrm{Cu-O1}}$ and $d_{\mathrm{Cu-O2}}$ increase, whereas the $d_{\mathrm{Cu-O3}}$ decreases, as depicted by the arrows in Fig. 8(e). The increases of $d_{\mathrm{Cu-O1}}$ and $d_{\mathrm{Cu-O2}}$ at T_{FE} are ≈0.8% and ≈2.5%, respectively, whereas the decrease of $d_{\mathrm{Cu-O3}}$ is ≈1.8% at T_{FE}. Below the structural transition, the $d_{\mathrm{Cu-O1}}$ shows an increasing trend, whereas the $d_{\mathrm{Cu-O2}}$ and $d_{\mathrm{Cu-O3}}$ decrease with decreasing temperature. The $d^b_{\mathrm{Cr-O}}$ with T is shown in Fig. 8(b). At the structural transition, the d^b_{Cr2-O1} contracts, below which it shows a decreasing trend with decreasing T. The contraction of the d^b_{Cr1-O2} and the elongation of the d^b_{Cr1-O3} are also shown in Fig. 8(b), which are further described by the arrows in Fig. 8(e). Here, the decreases in the d^b_{Cr2-O1} and d^b_{Cr1-O2} are ≈0.5% and ≈1.3%, respectively at T_{FE}. The increase in the d^b_{Cr1-O3} is ≈1.2%. Below the structural transition, the d^b_{Cr2-O1} decreases, whereas the values of d^b_{Cr2-O2} and d^b_{Cr2-O3} increase with decreasing temperature. The values of d^a_{Cr2-O2} and d^a_{Cr2-O3} are close and have similar temperature dependence, as depicted in Fig. 8(c). Here, the decreases in d^a_{Cr2-O2} and d^a_{Cr2-O3} are ≈0.3% and ≈0.2%, respectively. Similarly, the d^a_{Cr1-O1} decreases at the structural transition, below which it decreases with decreasing temperature. Here, the decrease in d^a_{Cr1-O1} at T_{FE} is ≈ 0.5%.

As displayed in Fig. 8(e), the $\mathrm{Cr2O_6}$ octahedron contacts, whereas the mixed distortions are observed for $\mathrm{Cr1O_6}$ octahedron and $\mathrm{CuO_4}$ tetrahedron. We note that the strongest distortion is ≈2.5% at T_{FE}, which is observed along the $d_{\mathrm{Cu-O2}}$ bond direction and is inclined nearly 10° with the crystallographic c axis. On the other hand, the distortion is ≈1.8% along the $d_{\mathrm{Cu-O3}}$ bond direction, which is 25.8° inclined with the c axis. For the $\mathrm{Cr1O_6}$, the distortions are significant as 1.2% and 1.3% for the d^b_{Cr1-O3} and d^b_{Cr1-O2}, respectively. Importantly, these two bond lengths make the angles of ≈18° and ≈38° with the c axis. The distortion of $\mathrm{Cr_2\,O_6}$ is much smaller than the rest of the two units. From the overall studies of distortions, we note that the major distortions are found close to c axis and thus the electric polarization direction is indicated close to the crystallographic c axis for $x = 0.2$.

Figure 9(a) shows the thermal variations of the bond angle Cu-O-Cr, which slowly increases with decreasing temperature above T_{FE}. Because of the distortions, the two bond angles, defined as α_1 and α_2 in Fig. 9(c), are possible below T_{FE}. Below the T_{FE}, the α_1 increases and α_2 decreases with decreasing temperature. Thermal variations of the bond angle Cr1-O-Cr2 bond angles are depicted in Fig. 9(b). Above T_{FE}, a slow decreasing trend is noticed with decreasing temperature. Below T_{FE}, the two bond angles defined as β_1 and β_2, as described in Fig. 9(c), show contrasting behavior. The β_1 decreases, whereas the β_2 increases with decreasing temperature.

Similarly, the high-Co-doped sample with $x = 0.8$ is thoroughly investigated by the synchrotron diffraction studies in the temperature range of 10–300 K. Temperature variation of the integrated intensity of the (200) diffraction peak is depicted in Fig. 10(a), which displays several signatures at different significant temperatures. It shows an anomaly around ≈247 K, as indicated by an arrow in the figure. With the further decrease in temperature, a maximum is observed around the T_{FE}. Another peak is also observed around T_N, which is followed by a sharp "dip" close to the T_s, proposing a strong magnetoelastic coupling. In accordance with

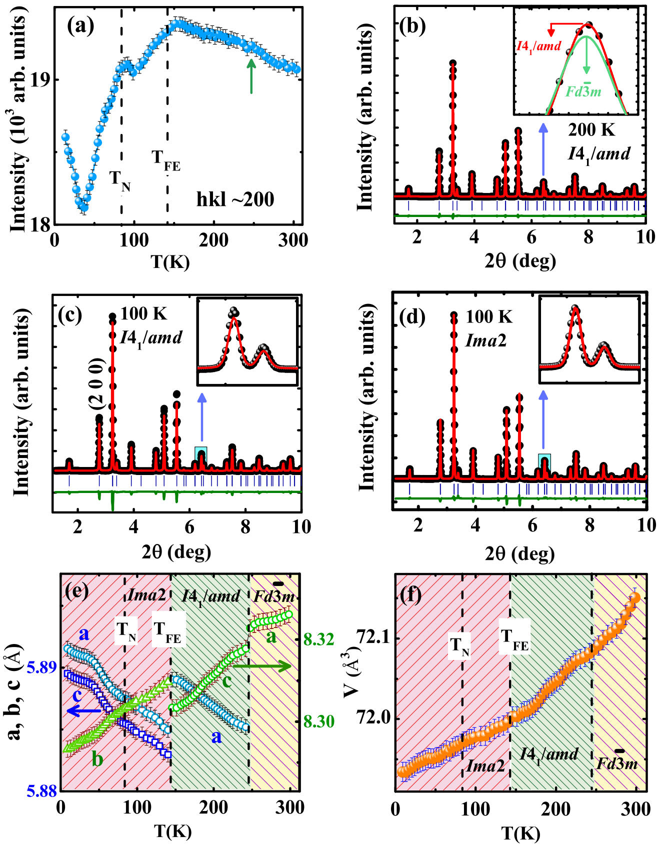

FIG. 10. (a) The T variation of the integrated intensity of the (200) peak. (b) Rietveld refinements of the diffraction pattern at 200 K using both the $Fd\bar{3}m$ and $I4_1/amd$ space groups. Inset shows a magnified peak with a better refinement using the $I4_1/amd$ space group. Rietveld refinements of the diffraction pattern at 100 K using the (c) $I4_1/amd$ and (d) $Ima2$ space groups. Insets further highlight the quality of the refinements in a small 2θ region. The T variations of the (e) lattice parameters, a, b, and c, and the (f) unit cell volume for $x = 0.8$.

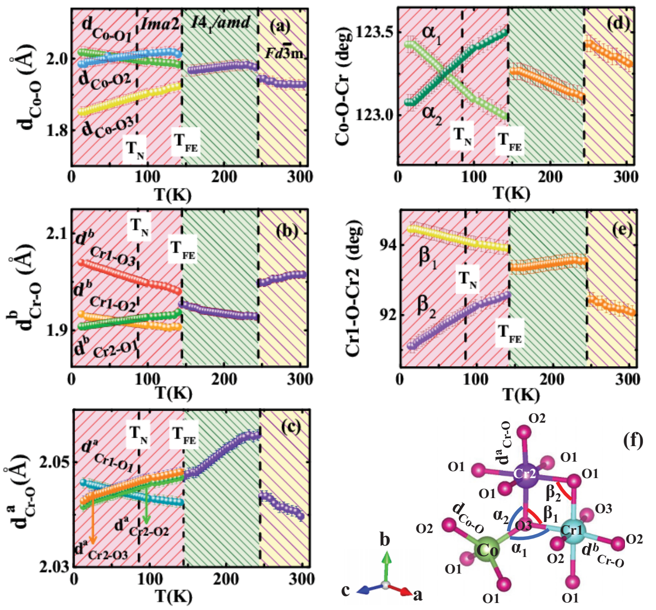

FIG. 11. The T variation of the (a) Cu-O bond length ($d_{\text{Cu-O}}$), (b) basal Cr-O bond length ($d^b_{\text{Cr}} - \text{O}$), (c) apex Cr-O bond length ($d^a_{\text{Cr-O}}$), (d) Co-O-Cr bond angle, and (e) Cr1-O-Cr2 bond angle. (f) Schematic representation of the details of the bond lengths and bond angles for $x = 0.8$.

the observed structural transition to a tetragonal $I4_1/amd$ structure around ≈853 K from the cubic $Fd\bar{3}m$ structure for the parent compound ($x = 0$) [14,16–24], a similar structural transition to a tetragonal $I4_1/amd$ structure is also observed at a much lower temperature of ≈247 K, around which an anomaly in the intensity plot is observed. An example of the Rietveld refinement of the diffraction pattern at 200 K using the $I4_1/amd$ space group is depicted in Fig. 10(b), where the inset shows the satisfactory fit of a selected small 2θ region. An unsatisfactory fit using the $Fd\bar{3}m$ space group is also shown in the inset by the curve with the green color. The refined atomic positions are given in Table II. In accordance with that observed structural transition at ≈168 K for $x = 0.2$, another structural transition to the polar $Ima2$ space group is proposed around ≈145 K for $x = 0.8$. The comparisons of the refinement of the diffraction pattern at 100 K using the $I4_1/amd$ and $Ima2$ space groups are depicted in Figs. 10(c) and 10(d), respectively. Insets of the corresponding figures clearly shows the selected peaks of the small 2θ region and confirms the better fit using the $Ima2$ than the $I4_1/amd$ space group. Thermal variation of the refined lattice parameters with the structural transitions at ≈247 K and ≈146 K are shown in Fig. 10(e). Three different temperature regions of structural phases are shown by three different patterns. An additional vertical broken straight line is also shown, indicating the temperature of magnetic ordering at ≈85 K. Temperature variation of unit cell volume is depicted in Fig. 10(f) and it shows a change of slope around the structural transitions.

In order to probe the structural distortions correlated with the appearance of the ferroelectric order microscopically, the bond lengths and bond angles between different atoms are investigated further. Figure 11 described the thermal variations of the bond lengths and the bond angles. Descriptions of the bond lengths and bond angles are summarized in Fig. 11(f). In Fig. 11(a), the thermal variations of $d_{\text{Co-O}}$ are shown with different characteristic features. Since Co is the major component at the tetrahedral site in $\text{Cu}_{0.2}\text{Co}_{0.8}\text{Cr}_2\text{O}_4$, we use Co only at the tetrahedral site for the simplicity. The $d_{\text{Co-O}}$ shows a discontinuous increase at 247 K, which is followed by an another discontinuous change at T_{FE}. Below T_{FE}, the $d_{\text{Co-O1}}$ increases with decreasing temperature. The $d_{\text{Co-O2}}$ decreases after an initial increase, whereas the $d_{\text{Co-O3}}$ decreases monotonically with decreasing temperature. The steplike increases of $d_{\text{Co-O1}}$ and $d_{\text{Co-O2}}$ are ≈0.8% and 2.3%, respectively. The steplike decrease of $d_{\text{Co-O3}}$ is ≈2.3 % at T_{FE}.

As depicted in Figs. 11(b) and 11(c), a considerable steplike decrease of d^b_{Cr-O} and a steplike considerable increase of $d^a_{\text{Cr-O}}$ are observed at 247 K, pointing a significant distortion of the CrO_6 octahedra. In addition, another intricate distortion is observed at T_{FE}. The changes in the basal $d_{\text{Cr-O}}$ bond lengths are observed at T_{FE}. The $d^b_{\text{Cr1-O3}}$ increases, whereas the $d^b_{\text{Cr1-O2}}$ and $d^b_{\text{Cr2-O1}}$ decrease at T_{FE}. The magnitude of changes are ≈1.5%, ≈2.3%, and ≈0.8% for d_{Cr1-O3}, $d_{\text{Cr1-O2}}$, and $d_{\text{Cr2-O1}}$, respectively. Below T_{FE}, the $d^b_{\text{Cr1-O3}}$ and $d^b_{\text{Cr2-O1}}$

show an increasing trend, whereas $d^{b}_{\mathrm{Cr1-O2}}$ shows a decreasing trend. Similarly, the changes in the apex bond lengths are observed at T_{FE}. The changes in d^{a}_{Cr2-O2} and $d^{a}_{\mathrm{Cr2-O3}}$ are nominal at T_{FE}, where a considerable decrease in d^{a}_{Cr1-O1} is observed at T_{FE}. The change in $d^{a}_{\mathrm{Cr1-O1}}$ is $\approx 0.2\%$. Below T_{FE}, the d^{a}_{Cr2-O2} and $d^{a}_{\mathrm{Cr2-O3}}$ decrease, whereas the $d^{a}_{\mathrm{Cr1-O1}}$ increases with decreasing temperature. Analogous to that observed for the distortion of the compound for $x = 0.2$ at T_{FE}, the distortions are considerable for the $d_{\mathrm{Co-O2}}$ and $d_{\mathrm{Co-O3}}$ in the $\mathrm{CoO_4}$ tetrahedron and the $d^{b}_{\mathrm{Cr2-O3}}$ and $d^{b}_{\mathrm{Cr2-O2}}$ in the $\mathrm{CrO_6}$ octahedron. Here, the $d_{\mathrm{Co-O2}}$, $d_{\mathrm{Co-O3}}$, $d^{b}_{\mathrm{Cr2-O2}}$, and $d^{b}_{\mathrm{Cr2-O3}}$ bonds make the angles of $\approx 10^\circ$, $\approx 25^\circ$, $\approx 38^\circ$, and $\approx 18^\circ$, respectively with the c axis and indicate that the electric polarization direction is close to the crystallographic c axis.

The bond angles are described in Fig. 11(f). The bond angle between the tetrahedron and octahedron, designated as the Co-O-Cr bond angle, and the bond angle between the two nearest neighboring octahedra, assigned as the Cr1-O-Cr2 bond angle, are depicted with temperature in Figs. 11(d) and 11(e), respectively. A steplike decrease in Co-O-Cr bond angle and a steplike increase in Cr1-O-Cr2 bond angle are noted at the high-temperature structural phase transition at 247 K. Below T_{FE}, the Co-O-Cr bond angles are redefined as α_1 and α_2, as described in Fig. 11(f). A steplike increase in α_2 and a steplike decrease in α_1 are observed at T_{FE}, below which a decreasing trend in α_2 and an increasing trend in α_1 are observed with decreasing temperature. At T_{FE}, the Cr1-O-Cr2 bond angle is redefined as β_1 and β_2, as described in Fig. 11(f). The β_1 and β_2 exhibit a steplike increase and decrease at T_{FE}, respectively, below which the β_1 increases and the β_2 decreases with decreasing temperature. The vertical broken straight line indicates the position of T_N in the figure, where a change in slope is noted in the α and β values, pointing to a magnetoelastic coupling. We further note that the Co-O-Cr bond angles change in the range of ≈ 123.0–123.5°, which is much smaller than the changes in the range of ≈ 91.5–94.3° for the Cr1-O-Cr2 bond angles. This indicates that the structural-distortion-driven tilting of the Cr octahedra is significant compared to the tilting of the Co tetrahedra.

In the current observation, the nature of the ferroelectric order in $\mathrm{Cu_{1-x}Co_xCr_2O_4}$ is distinctly different from the results of the extensively studied end member at $x = 1$ or $\mathrm{CoCr_2O_4}$ [27,45,46]. The FE order of $\mathrm{CoCr_2O_4}$ was reported at the conical magnetic order around 25 K, which is much below the long-range ferrimagnetic ordering around ≈97 K. Furthermore, unlike the members of $\mathrm{Cu_{1-x}Co_xCr_2O_4}$ family for $x < 1$, the $\mathrm{MnCr_2O_4}$ and $\mathrm{CoCr_2O_4}$ ($x = 1$) exhibit an isostructural transition at the ferroelectric order [41,47]. In contrast, the symmetry lowering is noted at T_{FE} for $x < 1$ in $\mathrm{Cu_{1-x}Co_xCr_2O_4}$, associated with $T_{\mathrm{FE}} > T_N$. Importantly, the value of P is nearly ≈300 times larger for $x = 0.8$ than the values for $\mathrm{CoCr_2O_4}$. In fact, the T_{FE} is much higher than the T_N associated with the larger P value for the entire series with $0 \leqslant x \leqslant 0.8$. The existence of the $\mathrm{Cu^{2+}}$ in the series of compounds is imperative, because the $\mathrm{Cu^{2+}}$ with the $3d^9$ electronic configuration is strongly a J-T active ion. The results are rather consistent with that observed for $\mathrm{Co_{0.8}Ni_{0.2}Cr_2O_4}$ with $T_{\mathrm{FE}} > T_N$, where the J-T active $\mathrm{Ni^{2+}}$ led to the crucial role [4]. The delicate interplay between orbital and structural degrees of freedom has been suggested in spinel compounds, where the J-T cations led to the structural phase transitions [6–8]. In those cases, the removal of the orbital degeneracy was settled in the ordering of the d orbitals and gave rise to the lowering of the crystal lattice symmetry. The compound with $x = 0$, i.e., $\mathrm{CuCr_2O_4}$, revealed a first-order structural transition from a high-temperature cubic structure in a $Fd\bar{3}m$ space group to a tetragonally distorted structure with a $I4_1/amd$ space group near 853 K [15]. The structural change has been proposed as a consequence of a transition from an orbitally disordered to an orbital ordered state driven by the J-T distortion of the $\mathrm{CuO_4}$ tetrahedron. Consistent with this suggestion, a structural transition to the orbitally ordered $I4_1/amd$ structure is anticipated for $x = 0.2$ above 300 K, which is beyond the maximum available limit of temperature for the synchrotron diffraction studies. However, with decreasing the quantity of the $\mathrm{Cu^{2+}}$ cation for $x = 0.8$, this structural transition temperature is reduced to 247 K, as evident in the thermal variation of the lattice parameters in Fig. 10(e).

Another low-temperature structural transition to a polar structure of $Ima2$ space group from the tetragonally distorted $I4_1/amd$ structure is noted for $x = 0.2$ and 0.8, which is crucial for the appearance of ferroelectric order. Temperature dependence of the phonon frequencies, as obtained from the optical conductivity spectra for $\mathrm{CuCr_2O_4}$, clearly demonstrated a splitting of the phonon frequencies around ≈170 K [7], at which we observe a ferroelectric order. A recent investigation of neutron diffraction studies of $\mathrm{CuCr_2O_4}$ confirmed a new collinear magnetic phase in between 125 K and 155 K [28]. The appearance of this new magnetic phase is relevant to the observed ferroelectricity around 170 K. The onset of magnetic ordering of the new magnetic phase and deviation of magnetization from the Curie-Weiss behavior close to T_{FE} [Fig. 3(a)] may be correlated to the proposed structural transition as well as ferroelectric ordering at 170 K, where possible exchange striction mechanism may lead to the ferroelectricity [42]. Possible exchange striction mechanism needs to be confirmed from the neutron diffraction studies in other members of $\mathrm{Cu_{1-x}Co_xCr_2O_4}$. We further note that the structural transition to a polar structure of $Ima2$ space group is confirmed around 168 and 146 K for $x = 0.2$ and 0.8, respectively, which lead to the ferroelectric order. Here, the control of the J-T distortion, driven by the substitution of the J-T active Cu by a non-Jahn-Teller active Co cation, causes a systematic shift of the structural transition to a polar $Ima2$ structure from the $I4_1/amd$ structure, which directs the tuning of the FE ordering temperature in the $\mathrm{Cu_{1-x}Co_xCr_2O_4}$ series.

In conclusion, the interplay between the J-T distortion driven orbital order and the structural instability correlated with the occurrence of ferroelectric order are invested in the $\mathrm{Cu_{1-x}Co_xCr_2O_4}$ series for $0 \leqslant x \leqslant 0.8$. In all the members, the FE orders are observed at much higher temperatures than the corresponding magnetic ordering temperatures. The structural transition to a polar $Ima2$ space group from the tetragonally distorted $I4_1/amd$ space group causes emergence of the ferroelectricity. The J-T active $\mathrm{Cu^{2+}}$ in $\mathrm{Cu_{1-x}Co_xCr_2O_4}$ is suggested to hold the key for the FE ordering at higher temperature and systematic change of the T_{FE} through the systematic substitution of $\mathrm{Cu^{2+}}$ by $\mathrm{Co^{2+}}$.

ACKNOWLEDGMENTS

S.G. acknowledges SERB, India (Project No. SB/S2/CMP-029/2014) for the financial support. S.G. also acknowledges DST, India, for the financial support to perform the experiment at PETRA III and DESY, Germany, for synchrotron diffraction studies (Proposal No. I-20170178).

---

[1] J. M. D. Coey, M. Viret, and S. von Molnár, Adv. Phys. **48**, 167 (1999).

[2] M. B. Salamon and M. Jaime, Rev. Mod. Phys. **73**, 583 (2001).

[3] M. R. Suchomel, D. P. Shoemaker, L. Ribaud, M. C. Kemei, and R. Seshadri, Phys. Rev. B **86**, 054406 (2012).

[4] A. A. Bush, V. Y. Shkuratov, K. E. Kamentsev, A. S. Prokhorov, E. S. Zhukova, B. P. Gorshunov, and V. I. Torgashev, Phys. Rev. B **85**, 214112 (2012).

[5] E. Jo, B. Kang, C. Kim, S. Kwon, and S. Lee, Phys. Rev. B **88**, 094417 (2013).

[6] M. Reehuis, M. Tovar, D. M. Többens, P. Pattison, A. Hoser, and B. Lake, Phys. Rev. B **91**, 024407 (2015).

[7] V. Kocsis, S. Bordács, D. Varjas, K. Penc, A. Abouelsayed, C. A. Kuntscher, K. Ohgushi, Y. Tokura, and I. Kézsmárki, Phys. Rev. B **87**, 064416 (2013).

[8] S. Bordaćs, D. Varjas, I. Keźsmaŕki, G. Mihaĺy, L. Baldassarre, A. Abouelsayed, C. A. Kuntscher, K. Ohgushi, and Y. Tokura, Phys. Rev. Lett. **103**, 077205 (2009).

[9] I. B. Bersuker, Phys. Rev. Lett. **108**, 137202 (2012).

[10] C. Xu, Y. Li, B. Xu, J. Íiguez, W. Duan, and L. Bellaiche, Adv. Funct. Mater. **27**, 1604513 (2017).

[11] G. Catalan, Phase Trans. **81**, 729 (2008).

[12] A. Aimi, D. Mori, K. Hiraki, T. Takahashi, Y. J. Shan, Y. Shirako, J. Zhou, and Y. Inaguma, Chem. Mater. **26**, 2601 (2014).

[13] Y. Zhang, H. J. Xiang, and M.-H. Whangbo, Phys. Rev. B **79**, 054432 (2009).

[14] J. D. Dunitz and L. E. Orgel, J. Phys. Chem. Solids **3**, 20 (1957).

[15] B. J. Kennedy and Q. Zhou, J. Solid State Chem. **181**, 2227 (2008).

[16] A. Wold, R. J. Arnott, E. Whipple, and J. B. Goodenough, J. Appl. Phys. **34**, 1085 (1963).

[17] Y. Kino and S. Miyahara, J. Phys. Soc. Jpn. **21**, 2732 (1966).

[18] E. Prince, Acta. Cryst. **10**, 554 (1957).

[19] Z. Ye, O. Crottaz, F. Vaudano, F. Kubel, P. Tissot, and H. Schmid, Ferroelectr. Lett. **162**, 103 (1994).

[20] W. A. Dollase and H. St. C. O'Neill, Acta Cryst. C **53**, 657 (1997).

[21] O. Crottaz, F. Kubel, and H. Schmid, J. Mater. Chem. **7**, 143 (1997).

[22] V. V. Ivanov, V. M. Talanov, and N. P. Shaberskaya, Inorg. Mater. **36**, 1167 (2000).

[23] M. Tovar, R. Torabi, C. Welker, and F. Fleischer, Phys. B (Amsterdam, Neth.) **385–386**, 196 (2006).

[24] K. Ohgushi, Y. Okimoto, T. Ogasawara, S. Miyasaka, and Y. Tokura, J. Phys. Soc. Jpn. **77**, 034713 (2008).

[25] R. Kumar, S. Rayaprol, V. Siruguri, Y. Xiao, W. Ji, and D. Pal, J. Magn. Magn. Mater **454**, 342 (2018).

[26] T. T. Gurgel, M. A. Buzinaro, and N. O. Moreno, J. Supercond. Novel. Magn. **26**, 2557 (2013).

[27] G. Lawes, B. Melot, K. Page, C. Ederer, M. A. Hayward, T. Proffen, and R. Seshadri, Phys. Rev. B **74**, 024413 (2006).

[28] K. Tomiyasu, S. Lee, H. Ishibashi, Y. Takahashi, T. Kawamata, Y. Koike, T. Nojima, S. Torii, and T. Kamiyama, arXiv:1803.06447.

[29] L. G. Wang, C. M. Zhu, Z. M. Tian, H. Luo, D. L. G. C. Bao, and S. L. Yuan, Appl. Phys. Lett. **107**, 152406 (2015).

[30] H. G. Zhang, Z. Wang, E. K. Liu, W. H. Wang, M. Yue, and G. H. Wu, J. Appl. Phys. **117**, 17B735 (2015).

[31] P. Mohanty, A. R. E. Prinsloo, B. P. Doyle, E. Carleschi, and C. J. Sheppard, AIP Adv. **8**, 056424 (2018).

[32] R. Kumar, R. Padam, D. Das, S. Rayaprol, V. Siruguri, and D. Pal, RSC Adv. **6**, 93511 (2016).

[33] G. J. Kumar, A. Banerjee, A. S. K. Sinha, Y. Su, K. Nemkovski, and C. Rath, J. Appl. Phys. **123**, 223905 (2018).

[34] A. Indra, K. Dey, S. Majumdar, I. Sarkar, S. Francoual, R. P. Giri, N. Khan, P. Mandal, and S. Giri, Phys. Rev. B. **95**, 094402 (2017).

[35] K. Dey, A. Karmakar, A. Indra, S. Majumdar, U. Rütt, O. Gutowski, M. v. Zimmermann, and S. Giri, Phys. Rev. B. **92**, 024401 (2015).

[36] A. Indra, K. Dey, J. K. Dey, S. Majumdar, U. Rutt, O. Gutowski, M. v. Zimmermann, and S. Giri, Phys. Rev. B. **98**, 014408 (2018).

[37] J. K. Dey, A. Chatterjee, S. Majumdar, A.-C. Dippel, O. Gutowski, M. V. Zimmermann, and S. Giri, Phys. Rev. B. **99**, 144412 (2019).

[38] H. J. Zhao, L. Bellaiche, X. M. Chen, and J. Íñiguez, Nat. Commun. **8**, 14025 (2017).

[39] Y. Shimakawa and Y. Kubo, Y. Nakagawa, S. Goto, T. Kamiyama, H. Asano, and F. Izumi, Phys. Rev. B. **61**, 6559 (2000).

[40] K. Dey, A. Indra, A. Chatterjee, S. Majumdar, U. Rütt, O. Gutowski, M. v. Zimmermann, and S. Giri, Phys. Rev. B **96**, 184428 (2017).

[41] K. Dey, S. Majumdar, and S. Giri, Phys. Rev.B. **90**, 184424 (2014).

[42] D. Khomskii, Physics **2**, 20 (2009).

[43] T. Kimura, Y. Sekio, H. Nakamura, T. Siegrist, and A. P. Ramirez, Nat. Mater. **7**, 291 (2008).

[44] B. J. Campbell, H. T. Stokes, D. E. Tanner, and D. M. Hatch, J. Appl. Crystallogr. **39**, 607 (2006).

[45] Y. Yamasaki, S. Miyasaka, Y. Kaneko, J. P. He, T. Arima, and Y. Tokura, Phys. Rev. Lett. **96**, 207204 (2006).

[46] Y. J. Choi, J. Okamoto, D. J. Huang, K. S. Chao, H. J. Lin, C. T. Chen, M. van Veenendaal, T. A. Kaplan, and S.-W. Cheong, Phys. Rev. Lett. **102**, 067601 (2009).

[47] G. T. Lin, Y. Q. Wang, X. Luo, J. Ma, H. L. Zhuang, D. Qian, L. H. Yin, F. C. Chen, J. Yan, R. R. Zhang, S. L. Zhang, W. Tong, W. H. Song, P. Tong, X. B. Zhu, and Y. P. Sun, Phys. Rev. B **97**, 064405 (2018).